Viscoelastic flow asymmetries in a helical static mixer and their impact on mixing performance.

T.P. John[a,*], R.J. Poole[b], A. Kowalski[c], C.P. Fonte[a]

[a] *Department of Chemical Engineering; The University of Manchester; Oxford Road; Manchester; M13 9PL; UK*
[b] *School of Engineering; The University of Liverpool; Brownlow Street; Liverpool; L69 3GH; UK*
[c] *Unilever R&D; Port Sunlight Laboratory; Quarry Road East; Bebington; Wirral; CH63 3JW; UK*

Abstract

Helical static mixers are often used during the processing of formulated products with complex rheological properties, such as viscoelasticity. Previous experimental studies have highlighted that increasing the viscoelasticity reduces the mixing performance of helical static mixers in the laminar flow regime. In this study, we use computational fluid dynamics to investigate the flow of a FENE-CR fluid in a helical static mixer. The results show clearly that the reduced mixing performance is caused by flow distribution asymmetries which develop at the mixer element intersections. The numerical results allow us to quantify the degree of asymmetry for the range of conditions studied, which is correlated with the quantified mixing performance for each simulation. The mixing is quantified using a Lagrangian particle tracking technique, and a new mixing index is defined based on the mean nearest distance between the two sets of tracked particles. The results show that the asymmetry parameter does not follow a pitchfork bifurcation, as it typically does for elastic instabilities in symmetrical geometries such as the cross-slot. For low values of the extensibility parameter, L^2, the flow remained (Eulerian) steady for all Reynolds Re and Weissenburg Wi numbers studied. At fixed Re and Wi, increasing L^2 causes the flow to become transient and greatly increases the magnitude of the asymmetry. The results presented in this study greatly help us to understand the effects that viscoelasticity can cause in mixing processes.

*Corresponding author
Email address: thomas.john@manchester.ac.uk (T.P. John)

1. Introduction

Static mixers are passive mixing devices which can be fixed into a pipeline in order to facilitate mixing of two or more components. They are particularly useful for mixing in flows in the laminar regime, where the naturally diffusive nature of inertially-driven turbulence cannot be utilised to promote mixing. Mixing at the molecular scale (micro-mixing) is essential for phenomena such as chemical reaction and is facilitated by molecular diffusion, which acts over significantly longer time-scales compared to the time-scales associated with turbulent dispersion. Thus, the primary function of a laminar mixing device is usually to reduce the scale of segregation of the components to a point where molecular diffusion can act to promote the micro-mixing in feasible time scales. The helical static mixer is one such commonly used static mixer for the mixing of highly viscous materials [24], which consists of a number of helical mixing elements arranged longditudinally in the pipe that split, rotate, stretch and recombine the flow. At the end of each mixer element, the consecutive element is twisted in the opposite direction and rotated 90 degrees around the pipe's longitudinal axis. If two fluids are initially joined with a Y-junction (i.e. for two initial striations), the number of striations should double, and hence the striation thickness should halve, every two mixing elements. Each combination of two mixing elements can be denoted as a flow period, since, across each combination two mixer elements, the flow is spatially periodic (provided it remains laminar) [41].

Many formulated products across various sectors such as personal care, home care, and food, exhibit complex rheological behaviour. In particular, many of these products exhibit viscoelasticity [6, 28]. Despite their frequent use for mixing of such rheologically complex materials, there have been only two previous studies (to the best of the authors' knowledge) regarding the mixing performance of a helical mixer for viscoelastic flows, both of which are experimental. Ramsay et al. [38] used Planar Laser Induced Fluorescence (PLIF) to visualise and quantify the mixing of a fluorescent dye in two different Boger fluids (water-glycerol solutions with 0.01 and 0.02 wt% of polyacrylamide (PAM)). The PLIF results showed that, for the two Boger fluids, the mixing performance after 6 elements of the mixer is drastically reduced when compared to the mixing of a Newtonian fluid (Glycerol), which the authors attribute to the generation of secondary structures in the flow by viscoelastic effects. The pressure drop across the mixer was found to increase for the two Boger fluids when compared to the Newtonian case. It is mentioned that this could be caused by the polymeric normal stresses present in the Boger fluids. Both the pressure drop and the striation patterns were strongly time-dependent for the Boger fluids but time-independent for the Newtonian fluid. The Reynolds number range in this study was between 10 and 30, and so, although the time-dependence of the flow is only observed for the Boger fluids, it can not be ascertained whether the time-dependence is purely elastic in nature or inerto-elastic.

Migliozzi et al. [30] also used PLIF to study mixing of viscoelastic materials in a helical static mixer. They used a Boger fluid (PAM dissolved in pure glycerol) and also two shear-thinning viscoelastic fluids (Xanthan Gum in water/glycerol solutions). They also found that the striation patterns produced by the viscoelastic flows were different to those produced by the Newtonian flows. They observe that increasing the viscoelasticity of the flow reduces the number of striations after two mixing elements (and thus reduces the mixing performance), and causes anomalous shapes to appear in the striation patterns. For moderate viscoelasticity, the striation patterns remain symmetric between the two halves of the cross-section. This symmetry is lost for higher degrees of viscoelasticity however. Time-dependence of the striation patterns was observed for flows beyond a critical value of the Deborah number, $De = \lambda/t$, where λ is the viscoelastic relaxation time and t is a characteristic time scale of the flow. For the Boger fluids, the onset of transient fluctuations in the mixing patterns occurred at approximately $De > 3$. This critical De was substantially lower for the Boger fluid than it was for the shear-thinning viscoelastic fluids, indicating that the Boger fluid is more prone to instabilities. It is explained by the authors that the PAM molecules in the Boger fluid exhibit higher extensibility than the Xanthan Gum molecules. Therefore, in flows with extension-dominated regions, the extensional stresses and viscosity grow larger for the Boger fluid than they do for the Xanthan Gum. This is reported to be the cause of the stronger time-dependence and lower critical De observed for the Boger fluids than for the shear-thinning fluids. For the shear-thinning fluids investigated, the striation patterns were still substantially different from the Newtonian ones, even though the time-dependence of the mixing patterns was much weaker or even negligible in some cases, indicating that the viscoelasticity can cause both steady and time-dependent changes in the flow and mixing performance of the helical mixer. In both of these previous experimental studies, only the mixing performance, quantified with the Coefficient of Variance (CoV), and pressure drop is explicitly measured. Changes brought about to the flow pattern within the mixer are only inferred from the changes in the striation patterns or pressure drop.

In the last few decades, there has been much research in the field of viscoelastic instabilities [13, 18, 42] and, in particular, flow asymmetries [15, 20, 21, 37, 39, 40, 43]. One of the first geometries to be studied in detail was the cross-slot geometry, now recognised as a bench-mark geometry for viscoelastic asymmetries [12]. In the cross-slot geometry, shown in Figure 1, the viscoelasticity causes a steady-state symmetry-breaking instability, which manifests as a super-critical pitchfork bifurcation [37] given by

$$\frac{\mathrm{d}\Delta}{\mathrm{d}t} = 0 = \Delta^3 - A(De - De_{\mathrm{crit}}), \tag{1}$$

where Δ is the parameter quantifying the degree of asymmetry and A is a constant to be determined empirically. Below the critical Deborah number De_{crit}, the flow bifurcates symmetrically ($\Delta = 0$) at the stagnation point in the center of the cross-slot. But then above De_{crit}, although reaching steady-state, the flow becomes asymmetric and the growth of Δ with increasing De follows a square-root trend. In bifurcation theory, in the case that a bias exists due to, for example, a slight asymmetry or imperfection in the geometry, an imperfection parameter h can be added to the right hand side of Equation (1). In this case, $\Delta \neq 0$ for $De < De_{\mathrm{crit}}$, and there is a gradual growth of $|\Delta|$ as $De \to De_{\mathrm{crit}}$, rather than an instantaneous change in Δ at De_{crit}. This is highlighted in Figure 2. In the cross-slot, for large enough De, the steady-state asymmetry transitions into a fully transient chaotic state [10], which is often referred to as elastic-turbulence [19, 27].

In the earlier investigations of the steady viscoelastic flow asymmetries in the cross-slot geometry, it was suggested that the driving mechanism for the asymmetry was related to the extensional flow and stresses at the stagnation point. It is observed in the regular cross-slot geometry that the onset of the asymmetry causes the flow near the stagnation point to change from being extensionally dominated to being shear dominated [2]. Also, the asymmetry causes a parameter named the "Couette correction" to drop with increasing De. The Couette correction is the pressure drop across the geometry after taking into account the pressure drop required for the viscoelastic channel flow in the absence of the cross-slot. As such, it represents, in a way, the energy requirement to drive the flow in the cross-slot. The drop in the value of the Couette correction with increasing De above the critical De indicates that the underlying driving mechanism for the asymmetry might be related to a drop in the energy requirement for the flow. However, the results from a more recent investigation by Davoodi et al. [14] suggest that asymmetry in the cross-slot is instead related simply to a classic "curved-pathlines" viscoelastic instability [33]. In the study of Davoodi et al. [14], a cylinder is added to the center of the cross-slot geometry, which removes the free stagnation point (and the associated strong extensional flow and stresses), however the viscoelastic asymmetry still occurs beyond a critical degree of viscoelasticity, indicating the asymmetry arises due to the curvature of the pathlines and high deformation rates near the channel corners.

Viscoelastic asymmetries have also been observed in a confined cylinder geometry, in which flow in a channel bifurcates around an obstructing cylinder. It has been found that increasing the Weissenberg number, $Wi = \lambda\dot{\gamma}$, where $\dot{\gamma}$ is a characteristic rate of strain, again led to a symmetry breaking instability, where the flow passed preferentially around one side of the cylinder in the channel [20, 21, 43]. This was observed with both experimental and

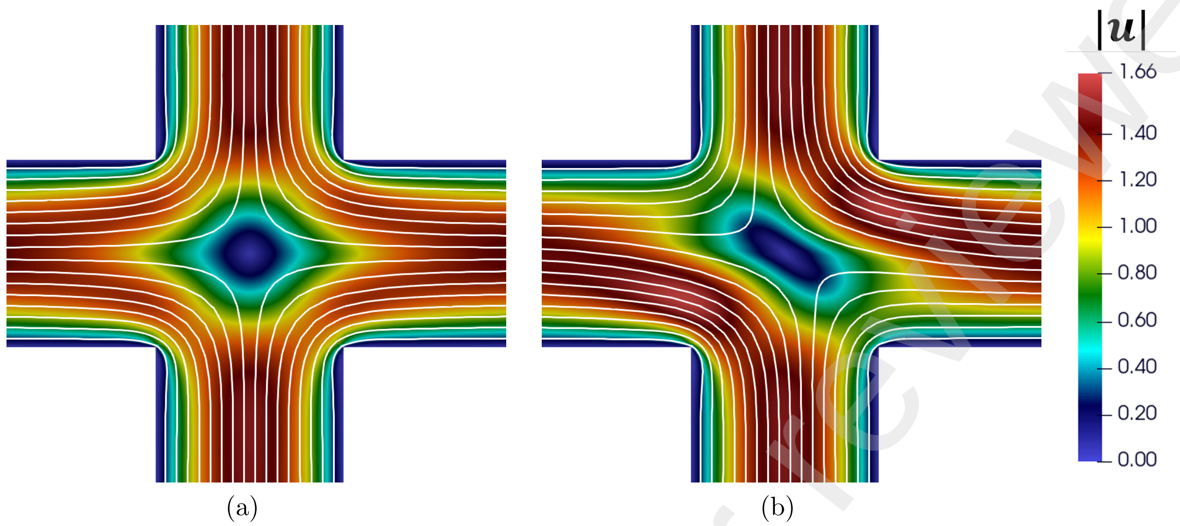

Figure 1: Contours of $|\boldsymbol{u}|$ for the cross-slot geometry before (a) and after (b) viscoelastic asymmetry is observed. Fluid pathlines are superimposed as white solid lines.

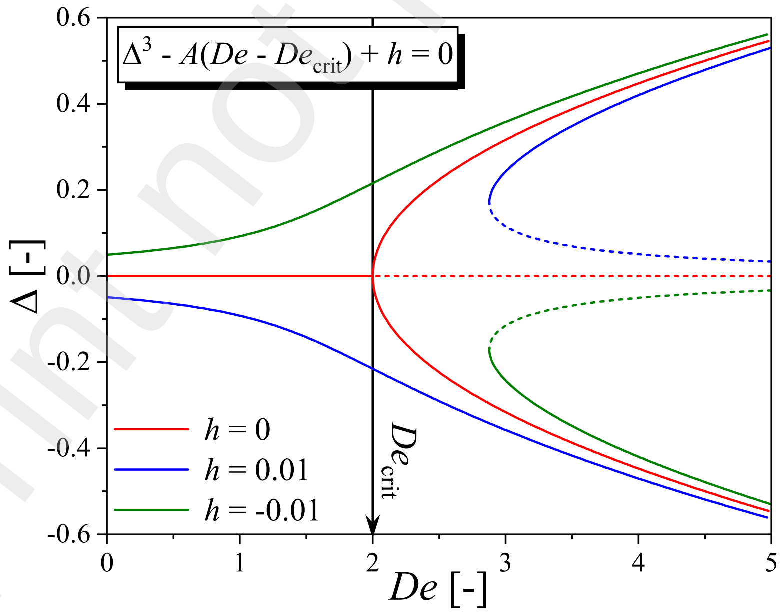

Figure 2: Examples of perfect (red) and imperfect (blue and green) pitchfork bifurcations. Solid lines show stables solution branches and dashed lines show un-stable solution branches

numerical methods. With regards to the choice of representing the degree of viscoelasticity with either De or Wi, De can be thought of as being related to the unsteadiness of the flow in a Lagrangian sense, whilst Wi represents the ratio of elastic and viscous forces (taking $[\tau_{11} - \tau_{22}]/\tau_{12}$ for the upper-convected Maxwell model under steady simple shear flow yields $2\lambda\dot{\gamma}$). For flows which are Eulerian and Lagrangian steady, it is the case that $De = 0$, and for geometries where the same length scale controls both the characteristic strain rate and time-scale, it is the case that $De = Wi$ and thus the choice for representing the degree of viscoelasticity is arbitrary. For Lagrangian unsteady flows with more than one important length scale, Wi and De are usually related simply via a geometric factor [36].

The confined cylinder geometry is not so dissimilar from the helical static mixer, in the sense that the flow in the helical mixer is also confined and bifurcates around the mixing elements at each element intersection point. The primary differences are that the helical mixer geometry twists the flow as it moves in the axial direction (hence the base flow is not symmetric), and that the edges of the mixing elements (at least those in this investigation) are square rather than circular. Whist the majority of investigations of viscoelastic flow asymmetries have employed symmetrical geometries, a recent numerical investigation by Kumar and Ardekani [26] employed an asymmetrical geometry. The geometry consisted of a channel with two confined cylinders, longitudinally arranged, where the front cylinder was fixed in the center of the channel width and the spanwise position of the rear cylinder was varied. When the rear cylinder is positioned centrally, the behaviour of the viscoelastic flow asymmetry follows closely that observed for other symmetrical geometries; the flow distribution around the cylinders is practically symmetrical until a critical Wi is reached, beyond which a sudden and sharp increase of the flow asymmetry is observed as Wi is increased. However, for the case where the rear cylinder is positioned off-center, the behaviour of the flow asymmetry is much different; even for low Wi there is a clear flow asymmetry around both cylinders and increasing Wi causes a more gradual increase in the degree of the asymmetry, rather than a sharp sudden increase. This would seem similar to the addition of an imperfection parameter h in the pitchfork bifurcation (see Figure 2), however this was not explored further in their study.

In this study, Computational Fluid Dynamics (CFD) is used, for the first time, to study viscoelastic fluid flows in the helical static mixer geometry, and the effect of viscoelasticity on the resulting mixing performance. In particular, we aim to understand and demonstrate how viscoelasticity can affect the performance of industrial process equipment. Gaining a better understanding of how viscoelasticity impacts the mixing quality in static mixers will allow for better design of equipment, processes, and formulated products. Previously, suggestions regarding the flow pattern of viscoelastic flows in the helical static mixer have been inferred from the mixing striation patterns observed with PLIF. With CFD, we can study details of the flow pattern inside the mixer and directly relate this to the change in the mixing performance.

2. Materials and methods

Here, we present the numerical methodology for the simulations, followed by an explanation of the methods used to quantify the mixing performance from the numerical results.

2.1. Governing equations

The continuity and momentum equations for in-compressible flow in the absence of external body forces are given respectively as

$$\nabla \cdot \boldsymbol{u} = 0, \tag{2}$$

$$\rho\left(\frac{\partial \boldsymbol{u}}{\partial t} + \boldsymbol{u} \cdot \nabla \boldsymbol{u}\right) = \nabla \cdot \boldsymbol{\sigma}, \tag{3}$$

where $\boldsymbol{\sigma}$ is the total stress tensor given as $\boldsymbol{\sigma} = -p\boldsymbol{I} + \boldsymbol{\tau}$, p is the pressure and $\boldsymbol{\tau}$ is the extra-stress tensor. We employ the FENE-CR (Finitely Extensibile Non-linear Elastic with

Chilcott and Rallison modification) model, first presented by Chilcott and Rallison [11], is used, which is given as

$$\boldsymbol{\tau} = \boldsymbol{\tau}_p + 2\eta_s \boldsymbol{D}, \tag{4}$$

$$\boldsymbol{\tau}_p + \lambda \overset{\triangledown}{\left(\frac{\boldsymbol{\tau}_p}{f} \right)} = 2\eta_p \boldsymbol{D}, \tag{5}$$

where $\boldsymbol{\tau}_p$ is the polymeric stress and $\boldsymbol{D}$ is the rate-of-strain tensor given by $\boldsymbol{D} = 1/2\left(\nabla \boldsymbol{u} + (\nabla \boldsymbol{u})^{\mathrm{T}}\right)$. η_s and η_p are the solvent and polymeric viscosities, respectively. The symbol $\overset{\triangledown}{(\ )}$ denotes the upper-convected time derivative, which, for a tensor $\boldsymbol{\psi}$, is given as

$$\overset{\triangledown}{\boldsymbol{\psi}} = \frac{\mathrm{D}\boldsymbol{\psi}}{\mathrm{D}t} - \boldsymbol{\psi} \cdot \nabla \boldsymbol{u} - \nabla \boldsymbol{u}^{\mathrm{T}} \cdot \boldsymbol{\psi}, \tag{6}$$

and represents the time rate of change written in a coordinate system which translates, rotates, and deforms with the material. It should be noted that the upper convected derivative in Equation (5) is acting on the whole term in the brackets, and not just on $\boldsymbol{\tau}_p$ as is the case in many other viscoelastic constitutive models. f is given by

$$f = \frac{L^2 + (\lambda/\eta_p)\mathrm{Tr}(\boldsymbol{\tau}_p)}{L^2 - 3}, \tag{7}$$

where L^2 is the extensibility parameter. We note that $\lim_{L^2 \to \infty} f = 1$, and in this limiting case the FENE-CR model reduces to the widely-used Oldroyd-B model.

In terms of material functions, the FENE-CR model has a constant shear viscosity in steady-shear, and so it can potentially be thought of as a Boger fluid [7] model. This is the primary feature of the FENE-CR model, which was modified empirically from the original FENE-P for this reason. The first normal stress difference, $N_1 = \sigma_{11} - \sigma_{22}$ (again, in steady-shear), grows quadratically with shear rate in the linear viscoelastic regime, and there is shear thinning of N_1 in the non-linear regime. In steady-state extensional flow, there is some thickening of the extensional viscosity with increasing strain rates, after which a plateau is reached. The value of the extensional viscosity at the plateau is proportional to L^2. For the Oldroyd-B model ($L^2 \to \infty$), there is no limiting of the extensional thickening and a singularity occurs. This is a well known short-coming of the Oldroyd-B model [42]. It should be noted here that since f is contained within the upper-convected derivative, the behaviour of the FENE-CR model in Eulerian or Lagrangian unsteady flows will differ from that implied from its steady material functions. This will be the case in the helical mixer geometry where even an Eulerian steady flow is un-steady in a Lagrangian sense. Moreover, the flow in the mixer section is complex (not pure shear, pure extension, or pure rotation), and it has been recently highlighted [44] that even the simplest viscoelastic model, the Oldroyd-B model, exhibits rheological behaviour which, in such flows, is more complex that that inferred from its material functions. We point this out just to highlight that the observed behaviour of the FENE-CR model in ideal steady flows can not necessarily be extrapolated to complex flows such as those in the static mixers.

We now introduce the dimensionless variables

$$t^* = t\frac{\mathcal{U}}{\mathcal{L}}, \quad \boldsymbol{u}^* = \boldsymbol{u}\frac{1}{\mathcal{U}}, \quad \boldsymbol{\tau}^* = \boldsymbol{\tau}\frac{\mathcal{L}}{\mathcal{U}(\eta_s + \eta_p)}, \quad p^* = p\frac{\mathcal{L}}{\mathcal{U}(\eta_s + \eta_p)}, \quad \nabla^* = \nabla\mathcal{L}, \tag{8}$$

and the following dimensionless groups

$$\beta = \frac{\eta_s}{\eta_s + \eta_p}, \quad Re = \frac{\rho\mathcal{U}\mathcal{L}}{(\eta_s + \eta_p)}, \quad Wi = \frac{\lambda\mathcal{U}}{\mathcal{L}}, \tag{9}$$

where $\mathcal{U}$ and $\mathcal{L}$ are characteristic velocity and length scales, respectively. Substituting the dimensionless variables into the momentum and constitutive equation, and dropping the asterisks for brevity, gives

$$Re\left(\frac{\partial \boldsymbol{u}}{\partial t} + \boldsymbol{u} \cdot \nabla \boldsymbol{u}\right) = -\nabla p + \beta \nabla^2 \boldsymbol{u} + \nabla \cdot \boldsymbol{\tau}_p, \tag{10}$$

$$\boldsymbol{\tau}_p + Wi\left(\frac{\overset{\triangledown}{\boldsymbol{\tau}_p}}{f}\right) = (1-\beta)(\nabla\boldsymbol{u} + \nabla\boldsymbol{u}^{\mathrm{T}}) \quad \text{where} \quad f = \frac{L^2 + \left(\frac{Wi}{(1-\beta)}\right)\mathrm{Tr}(\boldsymbol{\tau}_p)}{L^2 - 3}. \tag{11}$$

For the geometry used in this investigation, the helical static mixer, we define $\mathcal{U}$ and $\mathcal{L}$ as the inlet velocity u_{in} and pipe diameter D, respectively. There are three dimensionless parameters which, for a given geometry and value of L^2, can be varied, which are Re, Wi, and β. In this investigation, we use a constant value for β of 1/817 and we systematically vary Re and Wi for $L^2 = 50$, which is a typical value value of L^2 used for simulations with FENE constitutive models [31, 39]. The value of β chosen is close to that for typical fluids processed with helical static mixers in the laminar flow regime. We note here that the relatively low value of β is not representative of that for a "true" Boger fluid; the primary reason for the use of the FENE-CR model in this study is to remove the effects of shear-thinning and second normal stress differences etc, and not to explicitly attempt to model a Boger fluid. For $L^2 = 50$, Re was varied between 0.040 and 5.965, and Wi was varied between 0.010 and 1.500. Simulations were also run with increasing values of L^2 (up to $L^2 = 5000$) for $Re = 0.487$ and $Wi = 0.429$ in order to assess the effect of extensibility on the flow.

2.2. CFD simulations

All simulations were run using version 5.0 of RheoTool [34, 35], an open-source tool box based on OpenFOAM® [32]. OpenFOAM® uses the finite volume method to discretise the governing equations. The University of Manchester's Computational Shared Facility was used to run the simulations. Simulations were run with between 80 and 200 processors and took between a few hours to several days depending on the values of Re and Wi. In order to avoid the infamous high Weissenberg number problem, in which the polynomial interpolation fails to capture the exponential growth in stress, the log-conformation approach proposed by Fattal and Kupferman [17] is employed in this study. In this approach, the constitutive model is reformulated and the matrix logarithm of the conformation (or configuration) tensor $\boldsymbol{\Theta}$ is solved for, rather than $\boldsymbol{\tau}_p$. Spacial gradients of $\boldsymbol{\Theta}$ are better approximated by polynomials, and $\mathbf{\Theta}$ is also always positive-definite [1], which helps to stabilise the simulations. In the (dimensionless) FENE-CR model, $\mathbf{\Theta}$ is related to $\boldsymbol{\tau}_p$ by $\boldsymbol{\tau}_p = [(1-\beta)f_{\mathbf{\Theta}}/Wi](e^{\mathbf{\Theta}} - \mathbf{I})$ where $f_{\mathbf{\Theta}} = L^2/[L^2 - \text{tr}(e^{\mathbf{\Theta}})]$. The FENE-CR model in log-conformation form can be found in the RheoTool user guide [34].

Gradient terms were discretised using the Gauss Linear scheme, whilst the convective terms in both the momentum equation and FENE-CR model were discretised using the high-order CUBISTA scheme proposed by Alves et al. [4]. Highly accurate interpolation schemes are often needed for the disretisation of viscoelastic models, even for creeping flows, due to the absence of a diffusion-like term. Lower order schemes such as first-order upwind can introduce excessive numerical diffusion [5]. The Gauss Linear scheme with corrected surface normal gradient scheme was used for discretisation of Laplacian terms. The Euler scheme was used for time discretisation.

At the inlet of the pipe, a uniform and constant value for the fluid velocity and zero normal gradient of the pressure were set as boundary conditions. All components of $\mathbf{\Theta}$ were also specified as 0 at the inlet. At the outlet, the pressure was fixed at 0, and the *pressureInletOutletVelocity* boundary condition available in OpenFOAM® was used for the velocity, which is essentially a zero-gradient condition for purely outgoing flow. Although the flow at the outlet was always out-going, it was found that the *pressureInletOutletVelocity* condition helped to prevent convergence issues in some simulations. Zero normal gradient was also used at the outlet for $\mathbf{\Theta}$. At all solid walls, the no-slip condition was used for velocity, the zero-gradient condition was used for $\mathbf{\Theta}$, and the polymeric stress was linearly extrapolated. The fluid was initialised with a value of 0 for all variables (considering $\boldsymbol{\tau}_p$ rather than Θ).

To solve the equations, the Geometric agglomerated Algebraic MultiGrid (GAMG) solver was used for pressure with the Gauss Seidel smoother, and the *smoothSolver* was used for both the velocity and $\mathbf{\Theta}$ also with the Gauss Seidel solver. The tolerance and relative tolerance for both solvers respectively were 10^{-12} and 10^{-3}. All simulations with $L^2 = 50$

were run until steady-state had been reached. The two simulations with $L^2 = 500$ and $L^2 = 5000$ were unsteady and so were run for approximately 13λ, which was long enough for the unstable system to become fully-developed (i.e. by this point, fluctuations were clearly fluctuating around a steady mean). The time step was auto-adjusted using the maximum value of the Courant number. The Courant number is defined as $Co = \Delta_t \mathcal{T}$ where Δ_t is the time-step and $\mathcal{T}$ is a time scale based on the local cell flow scales. The maximum Co was varied between 0.4 for lower Wi cases and 0.05 for higher Wi cases. The change in the time-step should not affect any results for $L^2 = 50$ since they all reached steady-state. For the $L^2 = 5000$ simulation, which was unsteady, a time-step sensitivity test confirmed that the results were insensitive to the time-step at the maximum Co number we used.

2.3. Geometry and mesh

The mixer investigated in this study consists of 8 mixing elements (or 4 flow elements/periods). The diameter and length of the blades were fixed at 25.5 mm and 34.5 mm respectively (aspect ratio of roughly 1.35) and the thickness of the blades was 1.5 mm. These dimensions were used in the investigation conducted by Migliozzi et al. [30]. The entire pipe section simulated was 1 m in length and 25.5 mm in diameter. The center of the mixer section was located in the center of the pipe. Thus, there was always sufficient length between the inlet and the first mixer element for the flow to become fully-developed [16].

The mesh for the simulations, shown in Figure 3, was generated using ANSYS Meshing. To mesh the elements of the mixer, the sweep method was used to ensure that cells were hexahedral. The final mesh used for the simulations consisted of 4.93 million hexahedral cells. The mesh was chosen after performing a mesh independence study, the results of which can be found in the Supplementary Material. The mesh generated by ANSYS Meshing was converted for use in OpenFOAM® with the *fluentMeshToFoam* command.

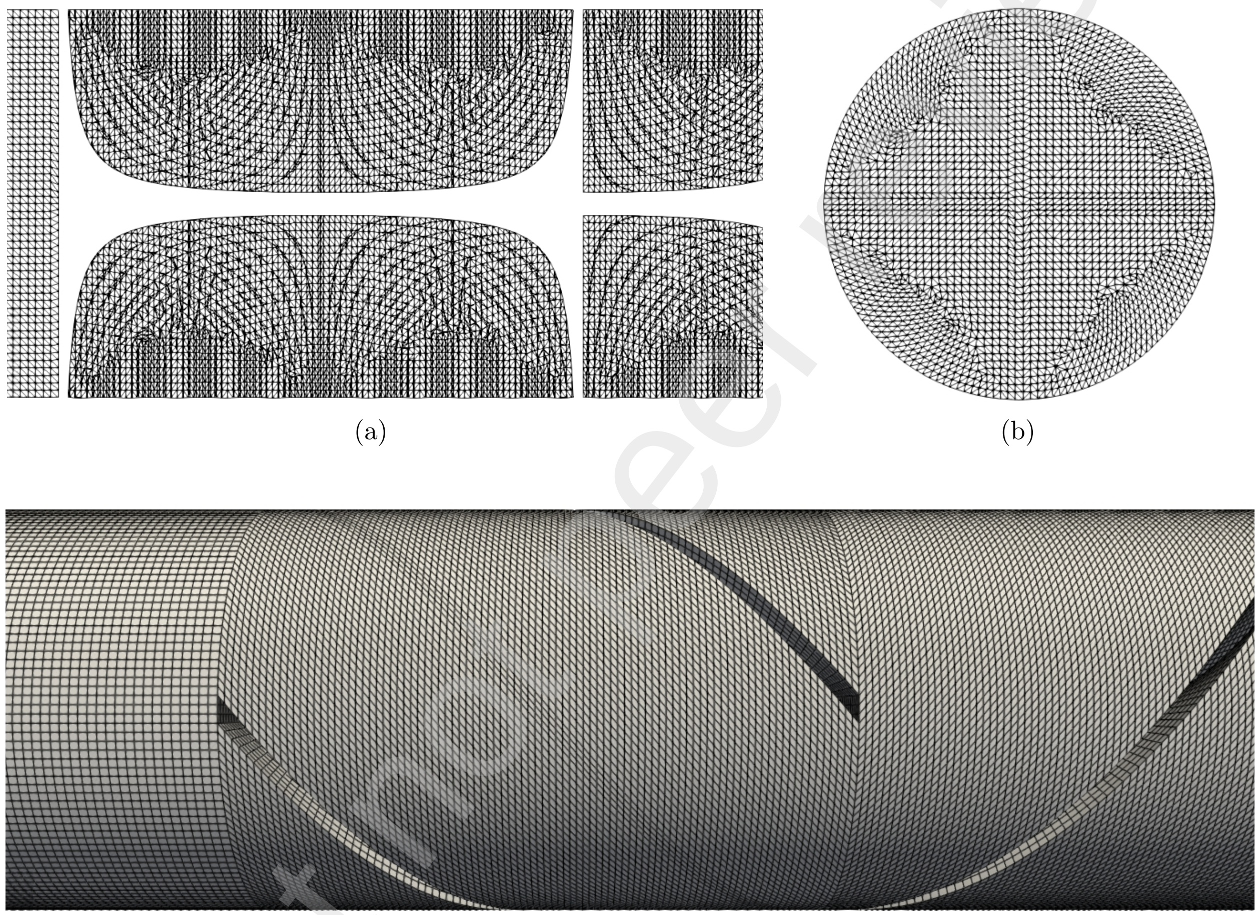

(a) (b)

(c)

Figure 3: Mesh used for the simulations. (a) 2D longitudinal slice in the mixer section. (b) Circular slice in the pipe section. (c) 3D view of the mesh at the beginning of the mixer section.

2.4. Quantification of mixing performance

In order to quantify the mixing performance, passive fluid elements were introduced to the flow at the beginning of the mixer geometry and their pathlines were analysed throughout the mixer. Starting at the entrance of the mixer geometry, roughly 50,000 elements were tracked using MATLAB® 2022a v9.12 [29] and Paraview v5.10 [3]. The elements are split into two groups, denoted by A and B, of roughly 25,000 elements each. The orientation of the two groups of elements was rotated at 90 degrees with respect to the first mixer element so that the elements did not bypass the first mixer element. This is shown in Figure 4. Circular slices (normal to the longitudinal direction) of the pathlines were taken at each element intersection point, and the mixing was then quantified.

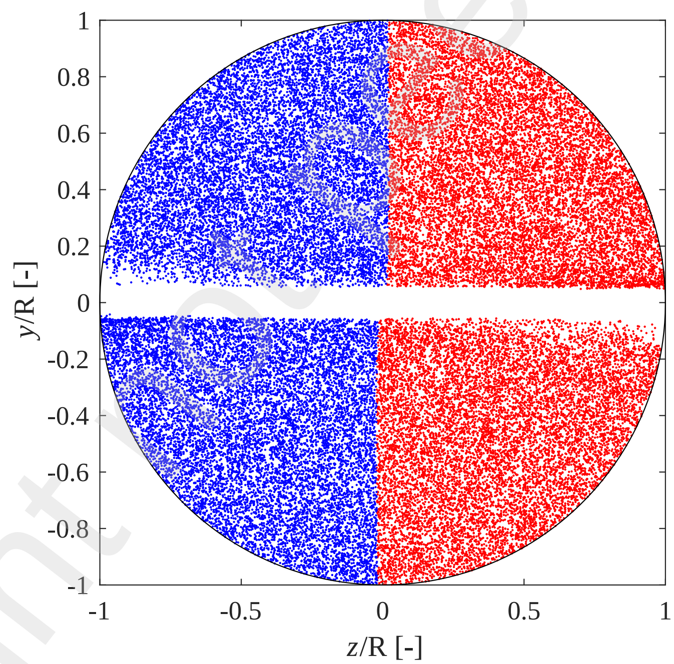

Figure 4: Initial positions of the tracked passive fluid elements at $n_e = 0$. The white horizontal rectangle shows the solid wall of the start of the first mixer element.

There are a number of methods for quantifying mixing using discrete particles or elements. For example, one could use the CoV or the Shannon Entropy, both of which have been employed previously in similar CFD mixing studies [8, 9, 22]. However, during the processing in ParaView, a number of pathlines were terminated, leading to some small blank patches in the mixing patterns. In order to avoid this affecting the results, we introduce a new method for the quantification of the mixing on 2D $y-z$ slices throughout the mixer geometry, implemented via MATLAB. We define the mixing index, I_m, as

$$I_m = \frac{1}{N_A}\sum_{i=1}^{N_A} \min[\mathbf{d}(\mathbf{P}_{A,i}, \mathbf{P}_B)], \tag{12}$$

where N_A is the number of fluid elements belonging to group A and $\mathbf{d}(\mathbf{P}_{A,i}, \mathbf{P}_B)$ is given by

$$\mathbf{d}(\mathbf{P}_{A,i}, \mathbf{P}_B) = \sqrt{(\mathbf{y}_B - y_{A,i})^2 + (\mathbf{z_B} - z_{A,i})^2}, \tag{13}$$

and represents an array consisting of the magnitudes of all of the 2D vectors in a $y-z$ plane pointing from the position $\mathbf{P}$ of particle i in group A (located in the 2D plane at $y_{A,i}$ and $z_{A,i}$) to the position of each of the particles in group B. The arrays $\mathbf{y}_B$ and $\mathbf{z}_B$ contain respectively the y and z positions of all elements in group B. As such, Equation (12) represents the mean distance from a particle in A to its nearest neighbour particle in B. This should scale closely with the striation thickness, which is commonly used to measure mixing performance in laminar mixing devices such as the helical static mixer [25, 41], and should be less influenced by the blank spaces caused by the termination of some of the pathlines. However, since the mixing here is being quantified with discrete methods, the index of mixing I_m will not decay to zero as the true mixing index in a continuous sense does, but will decay to a value determined by the total number of particles or pathlines used. Although this should be fairly obvious, it is noted here for clarity that $\min[\mathbf{d}(\mathbf{P}_{A,i}, \mathbf{P}_B)] = \min[\mathbf{d}(\mathbf{P}_{B,i}, \mathbf{P}_A)]$ and so the choice of which group of pathlines to index is arbitrary so long as $N_A \approx N_B$. Also, when results for the decay of I_m are presented, they will be normalised by the value of I_m obtained for the initial seeding of the pathlines, I_0, so that I_m/I_0 always decays from 1 at the start of the first mixing element.

3. Results and discussion

3.1. Steady flow asymmetries for $L^2 = 50$

In this sub-section, the main CFD results regarding the flow patterns generated in the mixer will be presented and discussed. The CFD results show that, as the viscoelasticity of the flow is increased, the flow bifurcates asymmetrically at the element intersections. This is shown for $Re = 0.04$ (i.e. negligible inertia) in Figure 5. For $Wi = 0.01$, the flow splits around the vertical wall of the mixing element relatively evenly. However, for $Wi = 1.5$, the flow clearly passes preferentially to one side of the vertical wall of the mixing element. Contours of u_x approaching $n_e = 5$ can be seen for $Re = 0.04$ and $Re = 5.96$ in Figures 6 and 7 respectively. For $Re = 0.04$ (Figure 6), the flow begins to preferentially flow below the up-coming horizontal mixing element as Wi is increased from 0.01 to 0.122. However, for $Wi > 0.122$, the flow distribution suddenly changes and the flow preferentially passes above the mixing element. It appears that the maximum value of u_x increases in both the upper and lower halves of the contour (above and below the up-coming horizontal intersection) as Wi is increased from 0.01 to 0.122, however, although it is not immediately obvious to the eye, the distribution of u_x in the upper half of the contour becomes slightly narrower and appears to be pushed slightly in an anti-clockwise direction, which matches the direction of the observed flow asymmetry for this range of Wi. For $Wi \geq 0.429$, the distribution of u_x in the lower quadrant seems to be almost "cut" diagonally (from bottom-left to upper-right or *vice versa*), where the flow above this diagonal line is forced above the up-coming horizontal element. For $Re = 5.96$, this "cutting" effect for $Wi \geq 0.429$ seems more pronounced and there appear to be sharp spatial gradients of u_x. Also, for $Re = 5.96$, the flow seems to pass preferentially above the horizontal mixing element as Wi is increased from 0.01 to 0.122, which is in contrast to the behaviour observed for $Re = 0.04$.

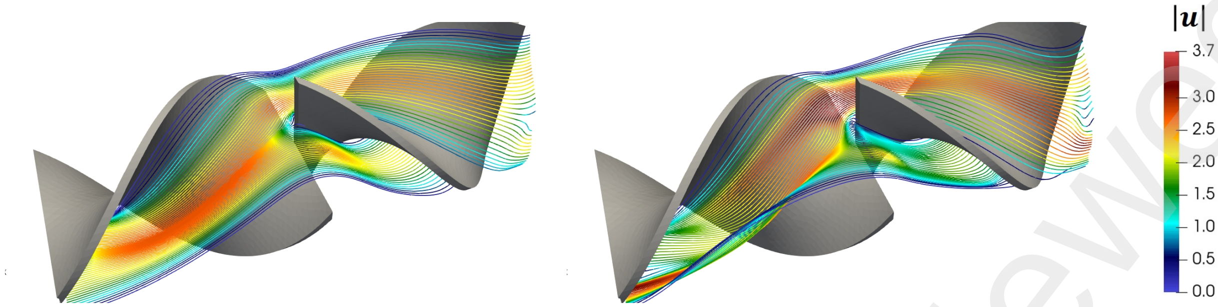

(a) (b)

Figure 5: Example of fluid pathlines around mixer elements 4 and 5 for (a) Wi = 0.01 and (b) Wi = 1.5. Re = 0.04 and L^2 = 50 for both cases. Pathlines are coloured by $|\boldsymbol{u}|$. Flow direction is from left to right. Pathlines are integrated (forward and backwards) from a line at the intersection of the two mixing elements.

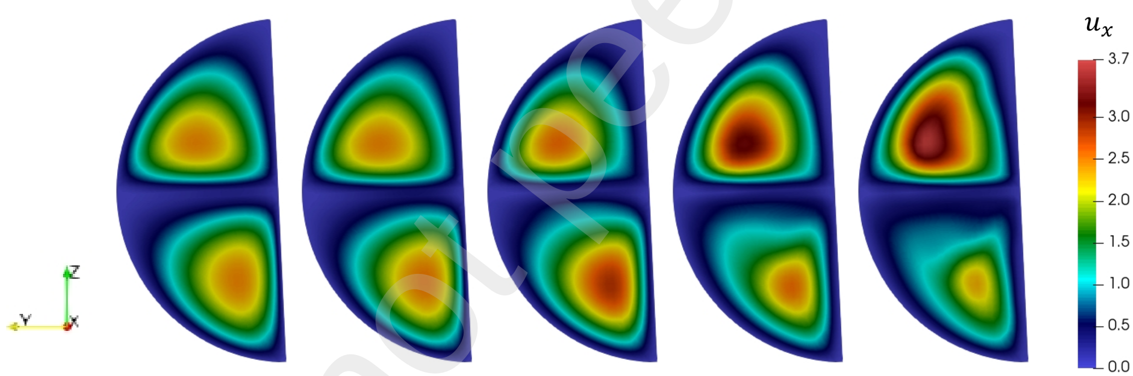

(a) Wi = 0.010 (b) Wi = 0.035 (c) Wi = 0.122 (d) Wi = 0.429 (e) Wi = 1.500

Figure 6: Contours of u_x for various Wi. Re = 0.040 and L^2 = 50. Slices are positioned at 5 mm before n_e = 5. The twisting direction of the element is clockwise. Fluid is flowing in the positive x direction (into the page).

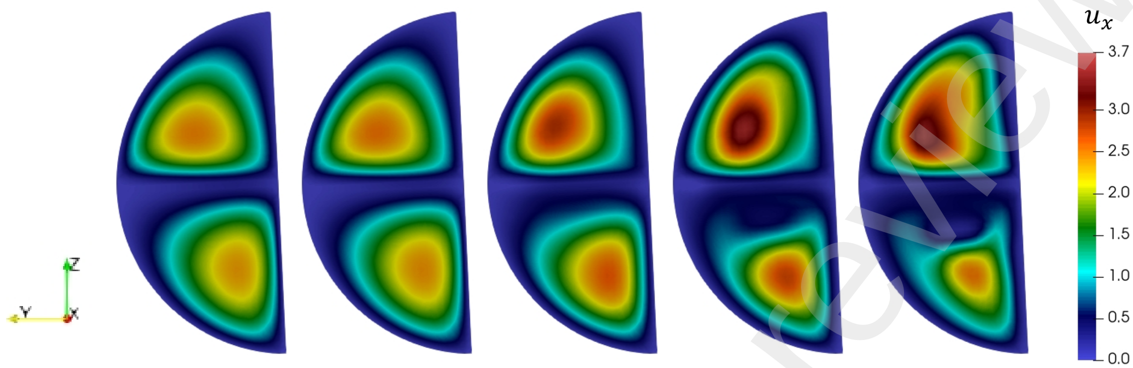

(a) $Wi = 0.010$ (b) $Wi = 0.035$ (c) $Wi = 0.122$ (d) $Wi = 0.429$ (e) $Wi = 1.500$

Figure 7: Contours of u_x for various Wi. $Re = 5.95$ and $L^2 = 50$. Slices are positioned at 5 mm before $n_e = 5$. The twisting direction of the element is clockwise. Fluid is flowing in the positive x direction (into the page).

In order to quantify the degree of asymmetry, the following parameter is defined

$$\Delta \equiv \frac{\max(u_x)_{s_i} - \max(u_x)_{s_j}}{\max(u_x)_{s_i} + \max(u_x)_{s_j}}, \tag{14}$$

where $\max(u_x)_{s_i}$ and $\max(u_x)_{s_j}$ are the maximum longitudinal velocities on the clipped surfaces s_i and s_j respectively. As such, $-1 < \Delta < 1$. Considering the clipped surfaces shown in Figure 8, a number of definitions for Δ can be introduced using adjacent surfaces. We introduce two of these and denote them as Δ_1 and Δ_2, which are given as

$$\Delta_1 \equiv \frac{\max(u_x)_{s_1} - \max(u_x)_{s_2}}{\max(u_x)_{s_1} + \max(u_x)_{s_2}}, \quad \Delta_2 \equiv \frac{\max(u_x)_{s_3} - \max(u_x)_{s_4}}{\max(u_x)_{s_3} + \max(u_x)_{s_4}}. \tag{15}$$

For all simulations using $L^2 = 50$, we were able to avoid having to re-define Δ for odd and even mixer elements, since it was apparent that $\max(u_x)_{s_1} \approx \max(u_x)_{s_3}$ and $\max(u_x)_{s_2} \approx \max(u_x)_{s_4}$. We checked $|\Delta_1 - \Delta_2|$ at all mixing element intersections for all simulations with $L^2 = 50$. The maximum value of $|\Delta_1 - \Delta_2|$ was found to be 1.1×10^{-3}, indicating that it is fair to assume $\Delta_1 = \Delta_2$. This anti-symmetry across the mixer element was also observed experimentally by Migliozzi et al. [30]. From here-on-in we will use $\Delta \equiv \Delta_1$ and we will not use the subscript when presenting results for Δ. With this choice of the definition of Δ, positive Δ means the flow is predominantly passing through the quadrant positioned in the twisting direction of the previous element, and negative Δ means the flow is predominantly passing through the quadrant positioned against the twisting direction of the previous element. For $\Delta = 0$, the bifurcation of the flow at the element intersections should be approximately symmetrical.

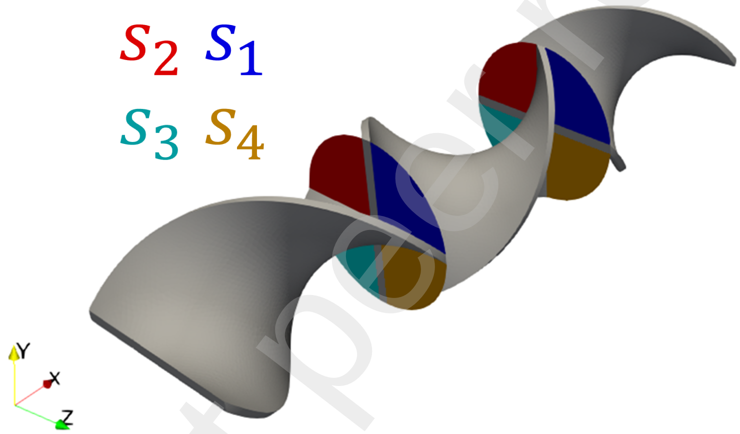

Figure 8: Part of the helical static mixer geometry with the clipped surfaces s_1, s_2, s_3, and s_4 which are used to define Δ. Flow direction is in the x-direction.

Figure 9 shows Δ as a function of Wi for each element number for $Re = 0.040, 0.487, 5.965$. In Figures 9a and 9b, Δ starts very close to zero for $Wi = 0.010$ (i.e. Newtonian) before becoming negative and increasing in magnitude up to $Wi = 0.122$. Beyond $Wi = 0.122$, the magnitude of Δ increases further, however the sign of Δ abruptly changes from negative to positive, as is indicated by the velocity contours in Figure 6. Δ is virtually constant for all elements for the lower values of Wi, but there is some change of Δ with the element number, specifically for the first few elements, for higher values of Wi. There appears to be no notable difference between the solutions for $Re = 0.04$ and $Re = 0.487$, indicating that the solution is practically independent of Re in this range.

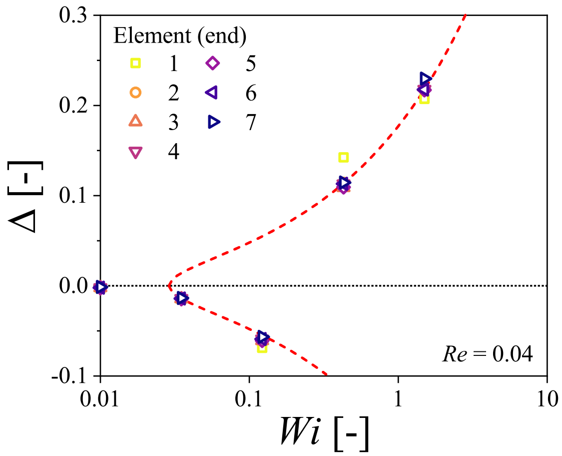

(a) Re = 0.040

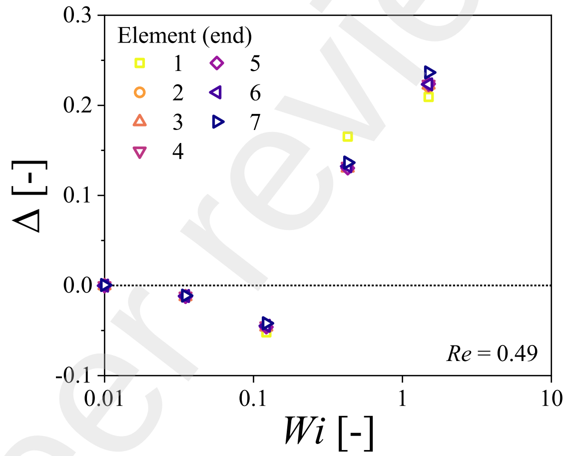

(b) Re = 0.487

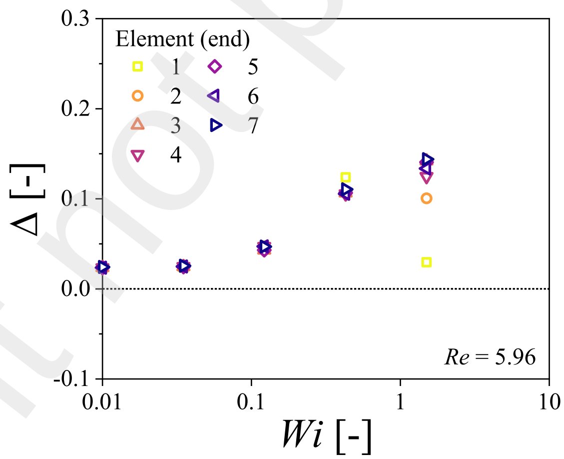

(c) Re = 5.965

Figure 9: Δ *versus* Wi for (a) Re = 0.040, (b) Re = 0.487, and (c) Re = 5.965. Red dashed line shows the fitting of a pitchfork-type bifurcation for n_e = 0.4

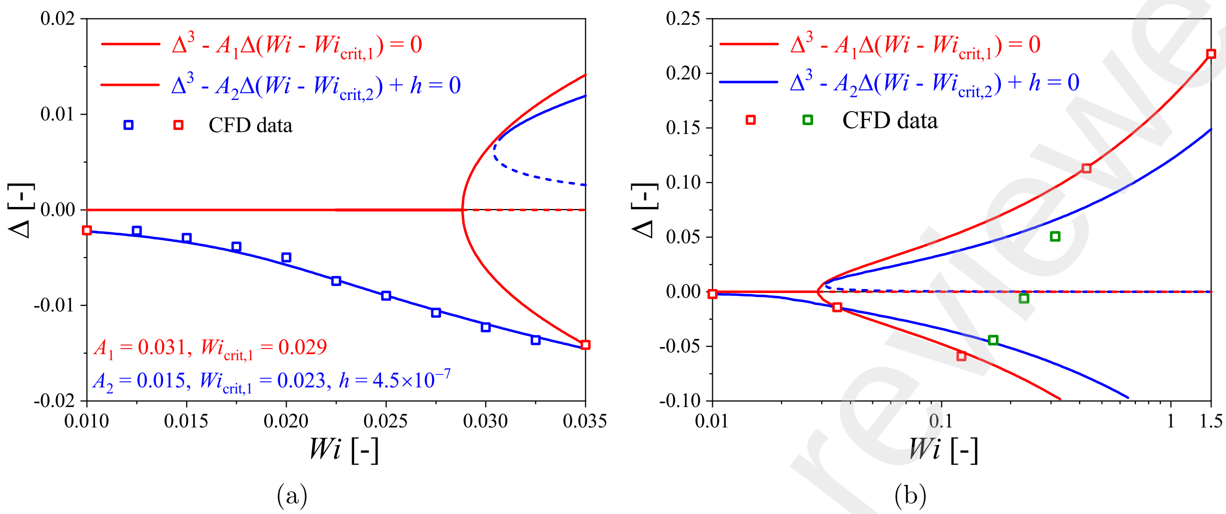

Figure 10: Δ at $n_e = 4$ *vs* Wi for the extra simulations ran to probe more closely the behaviour of Δ. (a) shows results between $Wi = 0.01$ and $Wi = 0.035$ (blue symbols) where the blue line represents a fitted imperfect pitchfork bifurcation. (b) shows the fitted imperfect pitchfork over the entire range of Wi, and extra simulations between $Wi = 0.122$ and $Wi = 0.429$ in green.

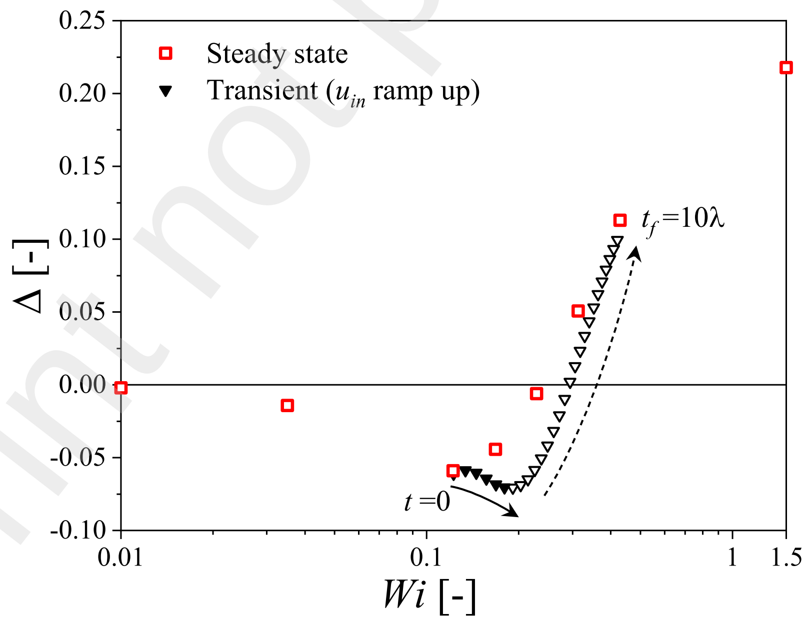

Figure 11: Results for simulation employing inlet velocity ramp. Red symbols show the steady-state simulations for $Re = 0.04$. Black symbols show the transient solution between $Wi = 0.122$ at $t = 0$ and $Wi = 0.429$ at $t_f = 10\lambda$. Filled symbols exhibit a downwards trend whilst hollow symbols follow the steady-state solution in an upwards trend.

There are multiple possible explanations for the behaviour observed in Figures 9a and 9b. One is that a viscoelastic instability occurs between $Wi = 0.01$ and $Wi = 0.035$, and both the downwards and upwards trends in Δ represent the two respective stable solution branches of a supercritical pitchfork bifurcation (either perfect or imperfect). To highlight this possibility, we have fitted the solution for a perfect pitchfork bifurcation ($\Delta = \pm\sqrt{A_1(Wi - Wi_{\text{crit}})}$) to the results in Figure 9a, which is shown by the red dashed line. We fitted the curve to the value of Δ at $n_e = 4$ and found $A_1 = 0.031$ and $Wi_{\text{crit}} = 0.029$. Since there is not enough data in Figure 9a to validate the onset of the square-root trend at the fitted value of Wi_{crit}, we ran 9 extra simulations spaced linearly between $Wi = 0.010$ and $Wi = 0.035$. The results for these simulations are displayed in Figure 10a. It is evident then that the asymmetry parameter does not exhibit a perfect pitchfork bifurcation (the red solid line) in the range of Wi investigated. This is highlighted by the gradual increase in $|\Delta|$ between $Wi = 0.010$ and $Wi = 0.035$ and also by the fact that Δ appears to asymptote to a small but finite value as $Wi \to 0$. As mentioned in Section 1, this gradual increase in the asymmetry parameter was also observed by Kumar and Ardekani [26] for flow around an asymmetric arrangement of two confined cylinders. Due to the asymmetric nature of the helical static mixer geometry, it would seem plausible that the flow asymmetry exhibits, instead, an imperfect pitchfork bifurcation. We have fitted the data shown in Figure 10a to an imperfect pitchfork bifurcation, shown by the blue solid line. The data appears to fit well between $Wi = 0.01$ and $Wi = 0.035$, however, in Figure 10b we show that Δ does not fit to the same imperfect pitchfork bifurcation for the entire range of Wi investigated. We also ran 3 extra simulations in between $Wi = 0.122$ and $Wi = 0.429$ to probe the apparent sharp transition from negative to positive Δ. These are shown by the green symbols in Figure 10b. If the asymmetry is indeed characterised by a pitchfork bifurcation, this transition from negative to positive Δ would likely just represent the CFD solver being able to access only the upper stable solution for $Wi > 0.122$. In Figure 10b, however, it is observed that the transition between negative and positive Δ is gradual, indicating that the flow is likely not characterised by either the perfect or imperfect pitchfork bifurcations.

Another potential explanation for the observed trend in Δ as Wi is increased is that the initial downwards trend in Δ for $Wi < 0.122$ represents some phenomenon related to viscoelasticity and streamline curvature; potentially a hoop stress or a similar elastic stress which can drive a change in the flow direction. In this case, the abrupt change in the sign of Δ, and hence direction of the asymmetry, between $Wi = 0.122$ and $Wi = 0.429$ might then represent the onset of an instability. To investigate this, we ran a simulation for $Re = 0.04$ where the initial condition was the steady-state solution for $Wi = 0.122$, and the inlet velocity was ramped such that $Wi = 0.122$ at time $t = 0$ and $Wi = 0.429$ at time $t = t_f$. We chose $t_f = 10\lambda$ so that the system remains close to steady-state at each point in time. It should be noted that, since the inlet velocity is increased, Re also increases from $Re = 0.04$ to $Re = 0.14$. However, as has been demonstrated, the solution is essentially independent of Re within this range. The results for this simulation are presented in Figure 11. At the start of the velocity ramp, the asymmetry continues on a downwards path despite the fact the steady-state solution starts to exhibit an upwards path. This indicates that beyond approximately $Wi = 0.122$, the system might still exhibit two stable solution branches, as a pitchfork-type bifurcation does. At approximately $Wi = 0.2$, the transient solution then begins to follow the trend exhibited by the steady-state solution. Potentially, a second stable steady-state solution path (downwards) exists beyond $Wi = 0.122$ but is just not accessible by the CFD solver.

For $Re = 5.96$, the sign of Δ is positive for all Wi studied, and for $Wi \to 0$, $|\Delta|$ tends to a larger value than it does for the lower Re cases. This shows that a degree of asymmetry is caused purely by inertia. Hobbs and Muzzio [23] simulated laminar Newtonian flows in a helical static mixer with CFD and also found that increasing Re led to an asymmetry at the element intersections. They also investigated the effect of the asymmetry on the mixing by using Lagrangian particle tracking to plot the Poincaré sections. They found that for intermediate Re (i.e. between creeping flow and transitional flow) the mixing was no longer globally chaotic, due to the flow asymmetries, as it was for creeping flow. In Figure 9c, for Re = 5.96, the maximum value of Δ reached as Wi is increased is significantly lower than for Re = 0.04 and 0.487, indicating that increasing inertia dampens these effects of viscoelasticity at high Wi. It has been shown for the cross-slot geometry that increasing Re dampens the viscoelastic instability and asymmetry [37]. There is also more variation in Δ with the element number for Re = 5.96 than for Re = 0.04 and Re = 0.487, particularly in the first 4 elements of the mixer. Figure 12 shows the contour of Δ for L^2 = 50 in the range of Re and Wi studied. Δ becomes most negative at moderate Wi (approximately 0.1) when $Re \to 0$, indicating that inertia acts to inhibit this effect of viscoelasticity in this region of $Re - Wi$ space. For $Re \approx 2$, Δ is no longer negative for the lowest values of Wi, however, the magnitude of Δ increases to a larger value (and more rapidly) with increasing Wi than it does for the largest values of Re. This indicates a complicated transition between the dominating effects of elasticity and inertia.

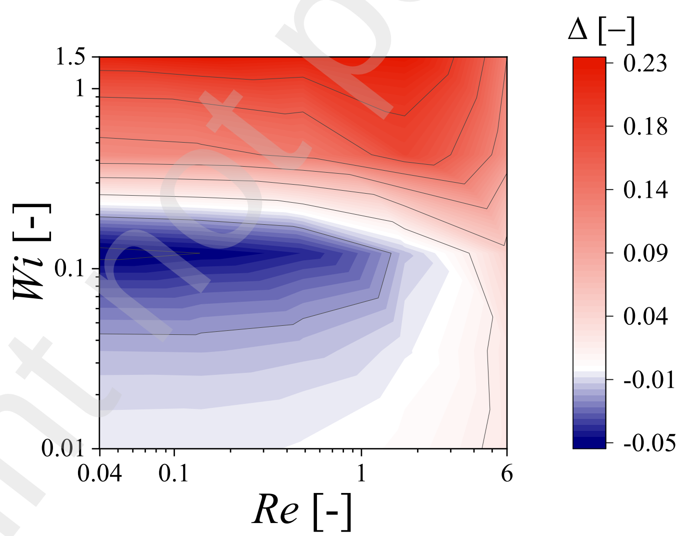

Figure 12: Contour of Δ for the range of Re and Wi studied. Note the data for the extra simulations shown in Figures 10 and 11 is not used to create this contour.

3.2. Effect of viscoelasticity on mixing performance

In this sub-section, we investigate the impact of the previously-discussed flow distribution asymmetries on the the mixing performance of the mixer for the range of Re and Wi investigated with $L^2 = 50$. As mentioned, the mixing performance is calculated using pathlines generated from the numerical flow-field results.

Figure 13 shows the mixing patterns predicted by the CFD simulations for $Re = 0.04$ at the ends of mixer elements 2, 4, and 6 for various Wi. For $Wi = 0.010$ (essentially creeping Newtonian conditions), the mixing patterns are very similar to the typical patterns generated by the helical static mixer for laminar flows reported in the literature [23, 41]. After 6 mixing elements, the striations are small and the distribution of striation thickness is narrow. As the viscoelasticity of the flow is increased, however, the mixing patterns change significantly. For $Wi = 1.5$, the pattern at the end of element 2 is changed slightly in shape from the lower Wi patterns, although the mixing quality might not seem so different. In the upper-left quadrant of plot, the striation of red particles furthest on the left appears to be squashed downwards; much less of this striation exists above the horizontal wall of the up-coming mixer element than it does for $Wi \leq 0.122$. Similarly, in the lower right quadrant, there is only one striation of red particles for $Wi = 1.5$, whereas there are two for $Wi \leq 0.122$. The direction of the movement of the striations as Wi is increased matches the direction of the flow asymmetry (note the co-ordinate system here is different to that in Figures 6 and 7). For the end of elements 4 and 6, there is a significant reduction in the mixing performance for $Wi = 1.5$. There is a significantly broader distribution of striation shape and size, with some very large striations (relatively speaking) remaining. We cannot infer that the direction of movement of striations is correlated with the asymmetry direction here since the striation patterns are much more complex. However, our results show that the significant change in the qualitative mixing performance is caused by the flow asymmetries present at the element intersection points discussed previously.

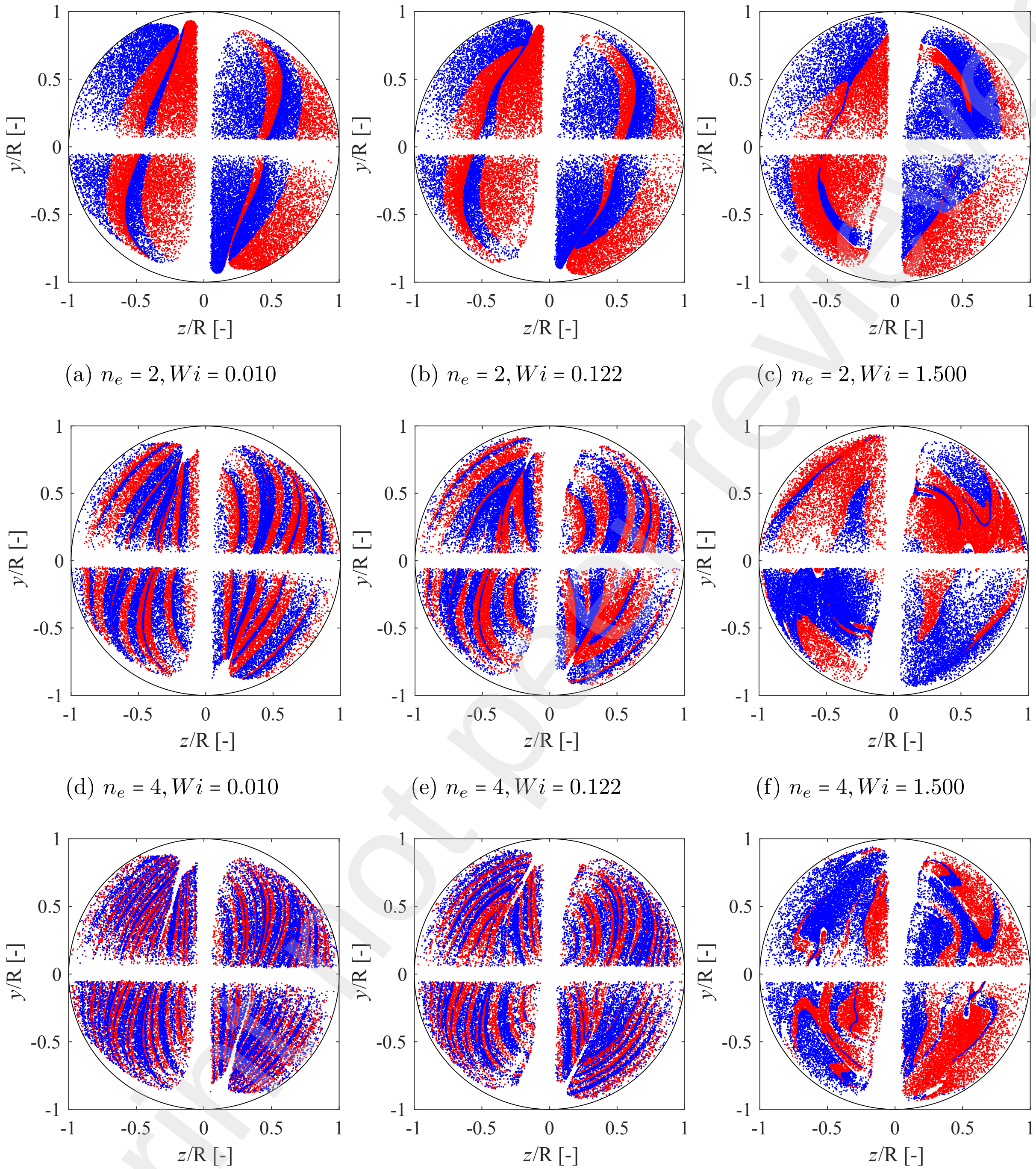

(a) $n_e = 2, Wi = 0.010$ (b) $n_e = 2, Wi = 0.122$ (c) $n_e = 2, Wi = 1.500$

(d) $n_e = 4, Wi = 0.010$ (e) $n_e = 4, Wi = 0.122$ (f) $n_e = 4, Wi = 1.500$

(g) $n_e = 6, Wi = 0.010$ (h) $n_e = 6, Wi = 0.122$ (i) $n_e = 6, Wi = 1.500$

Figure 13: Mixing patterns predicted by CFD simulations at $Re = 0.04$ for various values of Wi. Patterns shown at the end of elements 2 (a-c), 4 (d-f) and 6 (g-i).

Figure 14 shows I_m/I_0 *versus* n_e for the range of Wi and Re investigated with $L^2 = 50$. For both $Re = 0.04$ and $Re = 0.487$, I_m/I_0 decays practically as c^{-x} for the first three mixing elements when $Wi \leq 0.122$, which is natural since the mixing in the helical static mixer involves splitting and recombination of the flow,meaning the mixing index (or striation thickness etc) should ideally decay exponentially. As mentioned previously, the decay of I_m/I_0 slows for higher n_e even for the (practically) Newtonian case ($Wi = 0.010$), which is caused by the fact that the mixing is approaching the limit of that which can be quantified with the number of pathlines used. This does not impact the analysis or findings of this investigation since the effect of viscoelasticity on I_m/I_0 is easily distinguishable from this effect caused by using a finite number of pathlines.

For $Wi \leq 0.122$, the decay of I_m/I_0 is practically the same for varying Wi, with the exception that there is a small increase in I_m/I_0 at large n_e for $Wi = 0.122$, which is explained by the fact that the asymmetry grows in magnitude between $Wi = 0.010$ and $Wi = 0.122$. For $Wi \geq 0.429$, the decay of I_m/I_0 seems relatively unaffected by the viscoelasticity of the fluid for $n_e \leq 2$. However, for $n_e > 2$ there is a sudden and sharp change in the decay of I_m/I_0, where I_m/I_0 suddenly decays significantly slower for $n_e > 2$ than for $n_e \leq 2$. Since it has already been shown in Figure 9a that, for $Wi \geq 0.429$, the viscoelastic flow asymmetry is observed before $n_e = 2$, and is roughly constant for all n_e, the fact that I_m/I_0 is relatively unaffected by the increase in Wi before $n_e = 2$ cannot be attributed to an onset of the flow asymmetries at $n_e = 2$. Since the flow is symmetric (ie, not twisting) approaching the start of the first mixing element ($n_e = 0$), it is not be expected that the viscoelasticity of the flow would affect the mixing caused by the first element, except in the case of exceptionally large Wi (far beyond the range investigated in this study) where a purely symmetry-breaking instability would be expected as the flow bifurcates over the flat-edge of the first mixing element. This phenomenon would be similar in nature to the viscoelastic asymmetries observed for symmetric confined cylinder geometries [20, 21]. It is possibly the case, since the striations are relatively large at $n_e = 1$, that the observed flow asymmetry simply does not distort the fluid enough to have a significant impact on the decay of I_m/I_0 here. Similar results were obtained by Migliozzi et al. [30], who found that the CoV, measured experimentally using PLIF, was largely unaffected by the viscoelasticity of the fuid for the first two mixing elements, but then an increase in CoV (and hence reduction in mixing performance) was observed for increasing elasticity in the subsequent mixer elements. Since they used PLIF to investigate only the mixing performance, they were not able to explicitly relate the observed changes in the decay of the CoV to the changes in the flow kinematics induced by the viscoelasticity, however.

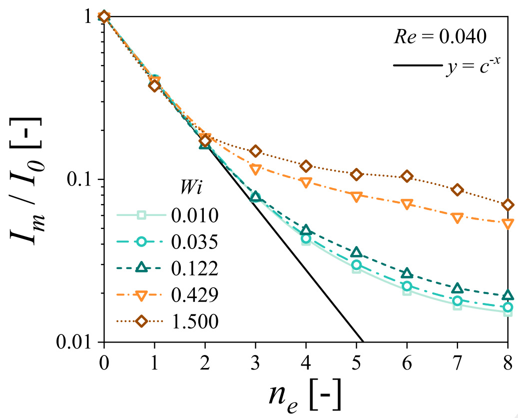

(a) Re = 0.04

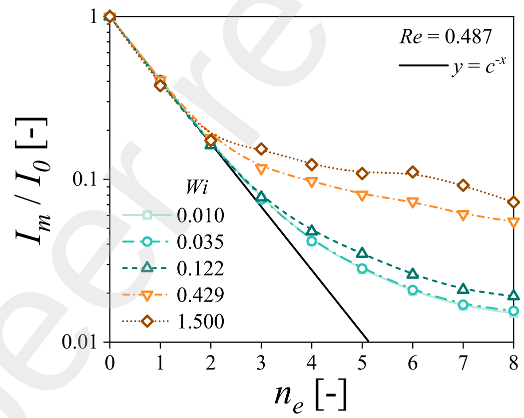

(b) Re = 0.487

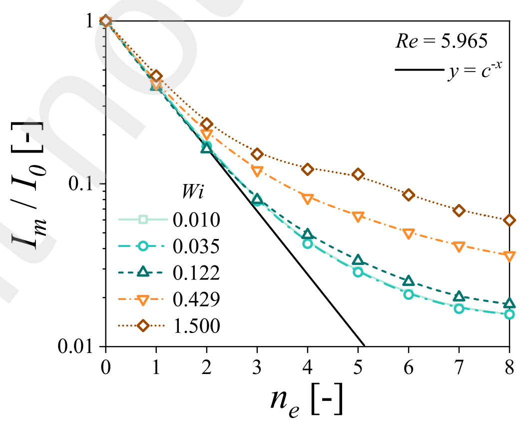

(c) Re = 5.96

Figure 14: Normalised mixing index, I_m/I_0, defined in Equations (12) and (13) *versus* n_e for varying Wi and for (a) Re = 0.04 and (b) Re = 5.96. Solid black line shows c^{-x}, where c = 2.45.

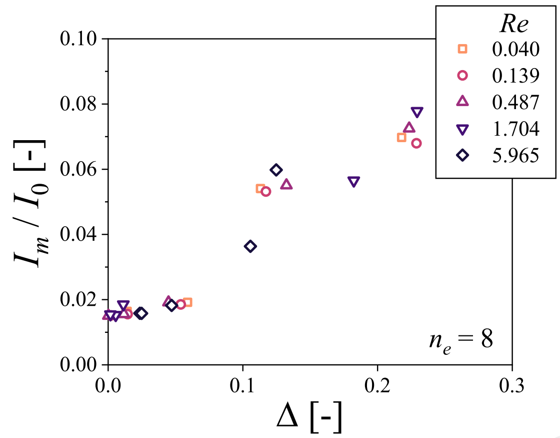

Figure 15: I_m/I_0 at $n_e = 8$ (mixer outler) *versus* Δ (computed at $n_e = 4$) for all $L^2 = 50$ simulations. Note that Δ is virtually constant for each mixer element after the first couple of elements.

Figure 15 shows I_m/I_0 at the outlet of the mixer section *versus* Δ (computed at $n_e = 4$) for all simulations where $L^2 = 50$ and the flow reached steady-state. There is a strong proportionality between the quantification of the asymmetry Δ and the mixing performance quantified by I_m/I_0, indicating that the asymmetry in the flow is indeed the cause of the change in the mixing performance, as expected. The non-zero y-intercept at $\Delta = 0$ is caused primarily by the fact a finite number of pathlines were used to quantify I_m, since the fitted exponential decay for low n_e (2.45^{-x}) gives a value of 7.7×10^{-4} for $n_e = 8$, which should be the value of I_m/I_0 in the case that $N_A \rightarrow infty$.

3.3. Effect of polymer extensibility

As mentioned previously, L^2 characterises the limit of the extensibility in the FENE constitutive models. Reducing L^2 in the FENE-CR model causes shear-thinning in N_1 to occur at lower Wi, and also inhibits the extensional-thickening behaviour. Thus, reducing L^2 should hypothetically lead to more stable viscoelastic flows for cases in which the extensibility causes large growths of polymeric stresses (e.g. flows with stagnation points).

In this study, we increase the value of L^2 between 50 and 5000 for fixed values of $Re = 0.49$ and $Wi = 0.429$. All results discussed previously were for cases in which $L^2 = 50$, and all of these simulations reached steady-state. It was observed in the helical static mixer that, for $L^2 > 50$, the flow became time-dependent. Figure 16 shows Δ as a function of time for $Re = 0.49$ and $Wi = 0.429$ for the three values of L^2 investigated. For $L^2 = 500$ the asymmetry, despite being time-dependent, seems to be fairly constant with respect to n_e for the elements further down the mixer, with $n_e = 4$ and $n_e = 7$ both showing the same behaviour in time. It should also be noted that for elements $n_e = 4$ and $n_e = 7$ the sign of Δ is opposite to those for $L^2 = 50$. For $L^2 = 5000$, the time dependence appears to be strong for $n_e = 7$, with large time fluctuations in Δ observed, particularly at $t/\lambda \approx 3$ and $t/\lambda \approx 11$. However, interestingly, Δ at $n_e = 4$ appears to be fairly steady in time, albeit much larger in magnitude. It is likely expected that for higher degrees of viscoelasticity, brought about by either increasing L^2 or Wi further, this time dependence will just grow stronger and more complex since the system should transition into a chaotic state of elastic turbulence [19].

Figures 17 and 18 show, respectively, contours of u_x at $n_e = 5$ for $L^2 = 500$ and $L^2 = 5000$. For $L^2 = 5000$, the asymmetry is significantly stronger than for $L^2 = 50$ and $L^2 = 500$, with the flow almost totally bypassing the upcoming element intersection (starting horizontally). The previous element is twisting in a clockwise direction, and so the fluid is predominantly flowing against the twisting direction (i.e. $\Delta < 0$).

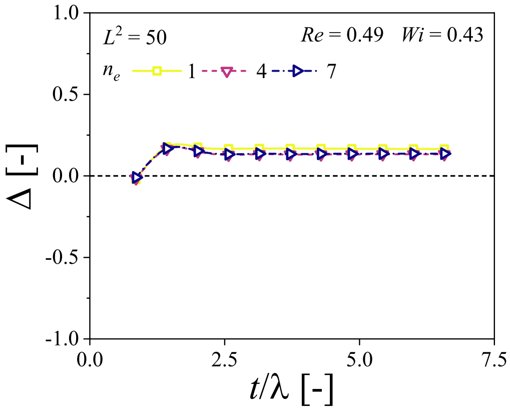

(a) $L^2 = 50$

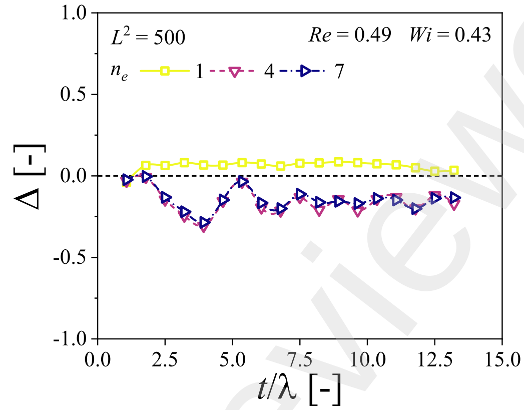

(b) $L^2 = 50$

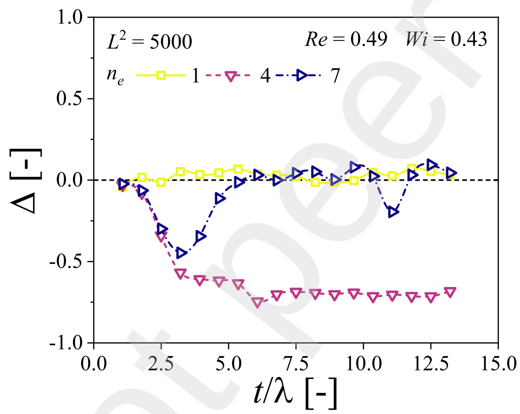

(c) $L^2 = 50$

Figure 16: Δ *versus* t/λ at various n_e for various values of L^2. Simulations are initialised with a stationary field at $t = 0$.

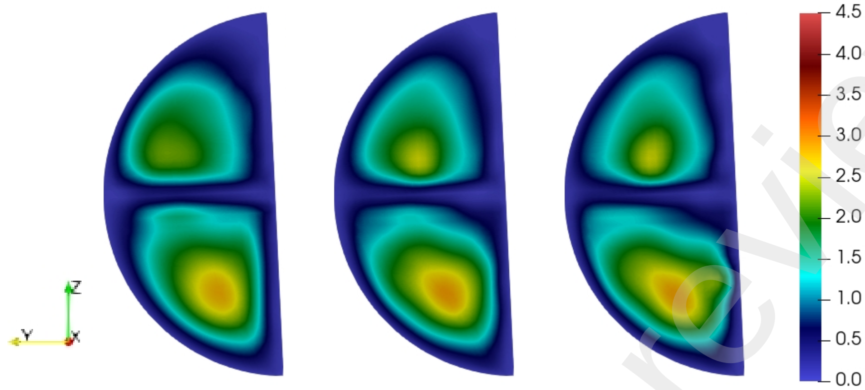

(a) $t/\lambda = 2.5$ (b) $t/\lambda = 7.5$ (c) $t/\lambda = 12.5$

Figure 17: Contours of u_x at $n_e = 5$ for $L^2 = 500$. Flow direction is into the page, and the flow is just approaching the horizontal edge of the upcoming element.

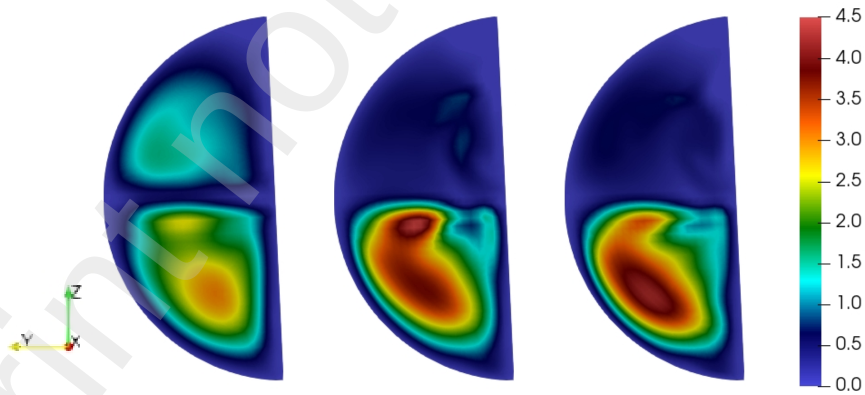

(a) $t/\lambda = 2.5$ (b) $t/\lambda = 7.5$ (c) $t/\lambda = 12.5$

Figure 18: Contours of u_x at $n_e = 5$ for $L^2 = 5000$. Flow direction is into the page, and the flow is just approaching the horizontal edge of the upcoming element.

Migliozzi et al. [30] report that the time-dependence of the mixing patterns, captured by PLIF, is totally suppressed in the helical static mixer geometry for solutions of Xanthan gum, whereas there is strong time-dependence for increasing elasticity with the PAA solutions (Boger fluid). They attribute this to the fact that the Xanthan gum solution is expected to have a near-constant extensional viscosity, whereas the PAA solution is expected to be strain-thickening in extensional flows. Ramsay et al. [38] also reports time-dependence of the flow of a PAA solution in the helical static mixer. Our results are in good agreement with the previous experimental results, since, by increasing L^2, the strain-thickening behaviour of the extensional viscosity is made more pronounced and the shear-thinning of N_1 is made less pronounced, giving rise to higher elastic normal stresses in complex flows (shear and extensional) such as those observed in the static mixer geometry.

4. Conclusions

We have used CFD to model viscoelastic fluid flow in a helical static mixer for a range of Reynolds and Weissenberg numbers. The results show that the viscoelasticity causes the flow to bifurcate asymmetrically at the intersections of the mixer elements, which reduces the mixing performance. Increasing viscoelasticity has been found to reduce the mixing performance of a helical static mixer in previous experimental studies, and so the numerical results from this study are in good agreement with experimental observations. However, with the CFD results, we are able to uncover the exact driving mechanism for the reduced mixing performance, having access to the necessary flow variables throughout the domain. The results greatly help us to understand how the complex rheology affects the mixing process in these flows.

The asymmetry at the element intersections has been quantified for the range of Re and Wi studied. It was shown that the sign of the asymmetry parameter (or the direction of the "bending" of the flow relative to the element twisting direction) exhibited complicated behaviour when varying Re and Wi. For low Re, the asymmetry parameter was negative and increased in magnitude with increasing Wi up until a critical Wi. Beyond this critical Wi, the sign of the asymmetry parameter changed abruptly, and the magnitude further increased with increasing Wi, indicating the possible presence of a viscoelastic instability. For high Re, the sign of the asymmetry parameter was always positive, and increased with increasing Wi. However, the highest magnitudes of the asymmetry parameter (at high Wi) were significantly lower for higher Re than for lower Re, indicating that inertia dampens the mechanism responsible for the asymmetry. This dampening of the viscoelastic asymmetry with increasing Re has been observed in simpler geometries previously. We show that the asymmetry parameter does not follow either a perfect or an imperfect pitchfork bifurcation. However, for low Re, and for $Wi > 0.122$, the results suggest that there may be two stable solution branches for the asymmetry parameter.

Increasing the limit of extensibility in the viscoelastic constitutive model (L^2) caused the simulation to change from steady to transient for intermediate values of $Re = 0.49$ and $Wi = 0.43$. Previous experimental studies also showed that viscoelastic materials which are expected to exhibit more extensibility showed stronger transient behaviour in the helical static mixer than those expected to exhibit less extensibility. And so, again, the numerical results agree with these experimental observations. The numerical results also show that increasing L^2 significantly increases the magnitude of the asymmetry, which is likely due to the increased extensional viscosity and normal stresses.

Acknowledgements

The authors acknowledge the financial support of the Center in Advanced Fluid Engineering for Digital Manufacturing, UK (CAFE4DM) project (Grant No. EP/R00482X/1)

References

[1] A M Afonso, P J Oliveira, F T Pinho, and M A Alves. The log-conformation tensor approach in the finite-volume method framework. *Journal of Non-Newtonian Fluid Mechanics*, 157:55–65, 2009. ISSN 0377-0257. doi: https://doi.org/10.1016/j.jnnfm.2008.09.007.

[2] A M Afonso, M A Alves, and F T Pinho. Purely elastic instabilities in three-dimensional cross-slot geometries. *Journal of Non-Newtonian Fluid Mechanics*, 165:743–751, 2010. ISSN 0377-0257. doi: https://doi.org/10.1016/j.jnnfm.2010.03.010.

[3] J P Ahrens, B Geveci, and C C Law. Paraview: An end-user tool for large-data visualization. In *The Visualization Handbook*, 2005.

[4] M A Alves, P J Oliveira, and F T Pinho. A convergent and universally bounded interpolation scheme for the treatment of advection. *International Journal for Numerical Methods in Fluids*, 41:47–75, 1 2003. ISSN 0271-2091. doi: https://doi.org/10.1002/fld.428. https://doi.org/10.1002/fld.428.

[5] M A Alves, P J Oliveira, and F T Pinho. Numerical methods for viscoelastic fluid flows. *Annual Review of Fluid Mechanics*, 53:509–541, 1 2021. ISSN 0066-4189. doi: 10.1146/annurev-fluid-010719-060107. doi: 10.1146/annurev-fluid-010719-060107.

[6] D Balzer, S Varwig, and M Weihrauch. Viscoelasticity of personal care products. *Colloids and Surfaces A: Physicochemical and Engineering Aspects*, 99:233–246, 1995. ISSN 0927-7757. doi: https://doi.org/10.1016/0927-7757(95)03144-3.

[7] D V Boger. A highly elastic constant-viscosity fluid. *Journal of Non-Newtonian Fluid Mechanics*, 3(1): 87–91, 1977. ISSN 0377-0257. doi: 10.1016/0377-0257(77)80014-1.

[8] M Camesasca, I Manas-Zloczower, and M Kaufman. Entropic characterization of mixing in microchannels. *Journal of Micromechanics and Microengineering*, 15:2038, 2005. ISSN 0960-1317. doi: 10.1088/0960-1317/15/11/007.

[9] M Camesasca, M Kaufman, and I Manas-Zloczower. Quantifying fluid mixing with the shannon entropy. *Macromolecular Theory and Simulations*, 15:595–607, 10 2006. ISSN 1022-1344. doi: https://doi.org/10.1002/mats.200600037. https://doi.org/10.1002/mats.200600037.

[10] D O Canossi, G Mompean, and S Berti. Elastic turbulence in two-dimensional cross-slot viscoelastic flows. *Europhysics Letters*, 129:24002, 2020. ISSN 0295-5075. doi: 10.1209/0295-5075/129/24002.

[11] M D Chilcott and J M Rallison. Creeping flow of dilute polymer solutions past cylinders and spheres. *Journal of Non-Newtonian Fluid Mechanics*, 29:381–432, 1988. ISSN 0377-0257. doi: https://doi.org/10.1016/0377-0257(88)85062-6.

[12] F A Cruz, R J Poole, A M Afonso, F T Pinho, P J Oliveira, and M A Alves. A new viscoelastic benchmark flow: Stationary bifurcation in a cross-slot. *Journal of Non-Newtonian Fluid Mechanics*, 214:57–68, 2014. ISSN 0377-0257. doi: https://doi.org/10.1016/j.jnnfm.2014.09.015.

[13] S S Datta, A M Ardekani, P E Arratia, A N Beris, I Bischofberger, G H McKinley, J G Eggers, J Esteban López-Aguilar, S M Fielding, A Frishman, M D Graham, J S Guasto, S J Haward, A Q Shen, S Hormozi, A Morozov, R J Poole, V Shankar, E S G Shaqfeh, H Stark, V Steinberg, G Subramanian, and H A Stone. Perspectives on viscoelastic flow instabilities and elastic turbulence. *Physical Review Fluids*, 7: 80701, 8 2022. doi: 10.1103/PhysRevFluids.7.080701.

[14] M Davoodi, A F. Domingues, and R J. Poole. Control of a purely elastic symmetry-breaking flow instability in cross-slot geometries. *Journal of Fluid Mechanics*, 881:1123–1157, 2019. ISSN 0022-1120. doi: 10.1017/jfm.2019.781.

[15] M Davoodi, G Houston, A Domingues, J Downie, D Dennis, M S N Oliveira, and R J Poole. Control of purely-elastic instabilities in cross-slot geometries. *Science Talks*, 3:100054, 2022. ISSN 2772-5693. doi: https://doi.org/10.1016/j.sctalk.2022.100054.

[16] F Durst, S Ray, B Ünsal, and O A Bayoumi. The development lengths of laminar pipe and channel flows. *J. Fluids Eng*, 127(6):1154–1160, June 2005. ISSN 0098-2202. doi: 10.1115/1.2063088.

[17] R Fattal and R Kupferman. Constitutive laws for the matrix-logarithm of the conformation tensor. *Journal of Non-Newtonian Fluid Mechanics*, 123:281–285, 2004. ISSN 0377-0257. doi: https://doi.org/10.1016/j.jnnfm.2004.08.008.

[18] F J Galindo-Rosales, L Campo-Deaño, P C Sousa, V M Ribeiro, M S N Oliveira, M A Alves, and F T Pinho. Viscoelastic instabilities in micro-scale flows. *Experimental Thermal and Fluid Science*, 59: 128–139, 2014. ISSN 0894-1777. doi: https://doi.org/10.1016/j.expthermflusci.2014.03.004.

[19] A Groisman and V Steinberg. Elastic turbulence in a polymer solution flow. *Nature*, 405:53–55, 2000. ISSN 1476-4687. doi: 10.1038/35011019.

[20] S J Haward, C C Hopkins, and A Q Shen. Asymmetric flow of polymer solutions around microfluidic cylinders: Interaction between shear-thinning and viscoelasticity. *Journal of Non-Newtonian Fluid Mechanics*, 278:104250, 2020. ISSN 0377-0257. doi: https://doi.org/10.1016/j.jnnfm.2020.104250.

[21] S J Haward, C C Hopkins, S Varchanis, and A Q Shen. Bifurcations in flows of complex fluids around microfluidic cylinders. *Lab on a Chip*, 21:4041–4059, 2021. ISSN 1473-0197. doi: 10.1039/D1LC00128K.

[22] D M Hobbs and F J Muzzio. The kenics static mixer: a three-dimensional chaotic flow. *Chemical Engineering Journal*, 67:153–166, 1997. ISSN 1385-8947. doi: https://doi.org/10.1016/S1385-8947(97)00013-2.

[23] D M Hobbs and F J Muzzio. Reynolds number effects on laminar mixing in the kenics static mixer. *Chemical Engineering Journal*, 70:93–104, 1998. ISSN 1385-8947. doi: https://doi.org/10.1016/S0923-0467(98)00065-7.

[24] A W Etchells III and C F Meyer. Mixing in pipelines, 11 2003. Wiley Online Books.

[25] S A Jaffer and P E Wood. Quantification of laminar mixing in the kenics static mixer: An experimental study. *The Canadian Journal of Chemical Engineering*, 76:516–521, 6 1998. ISSN 0008-4034. doi: https://doi.org/10.1002/cjce.5450760323. https://doi.org/10.1002/cjce.5450760323.

[26] M Kumar and A M. Ardekani. Viscoelastic instability in an asymmetric geometry. *The European Physical Journal Special Topics*, 2022. ISSN 1951-6401. doi: 10.1140/epjs/s11734-022-00657-9.

[27] R G Larson. Turbulence without inertia. *Nature*, 405:27–28, 2000. ISSN 1476-4687. doi: 10.1038/35011172.

[28] G Lorenzo, N E Zaritzky, and A N Califano. Viscoelastic characterization of fluid and gel like food emulsions stabilized with hydrocolloids. *Procedia Food Science*, 1:281–286, 2011. ISSN 2211-601X. doi: https://doi.org/10.1016/j.profoo.2011.09.044.

[29] MATLAB. *version 9.12.0 (R2022a)*. The MathWorks Inc., Natick, Massachusetts, 2022.

[30] S Migliozzi, L Mazzei, and P Angeli. Viscoelastic flow instabilities in static mixers: Onset and effect on the mixing efficiency. *Physics of Fluids*, 33:013104, 1 2021. ISSN 1070-6631. doi: 10.1063/5.0038602. doi: 10.1063/5.0038602.

[31] P J Oliveira. Alternative derivation of differential constitutive equations of the oldroyd-b type. *Journal of Non-Newtonian Fluid Mechanics*, 160:40–46, 2009. ISSN 0377-0257. doi: https://doi.org/10.1016/j.jnnfm.2008.11.013.

[32] OpenCFD. *OpenFOAM - The Open Source CFD Toolbox - User's Guide*. OpenCFD Ltd., United Kingdom, 1.4 edition, 11 April 2007.

[33] P Pakdel and G H. McKinley. Elastic instability and curved streamlines. *PRL*, 77(12):2459–2462, September 1996. doi: 10.1103/PhysRevLett.77.2459.

[34] F Pimenta and M A Alves. rheotool. `https://github.com/fppimenta/rheoTool`, 2016.

[35] F Pimenta and M A Alves. Stabilization of an open-source finite-volume solver for viscoelastic fluid flows. *Journal of Non-Newtonian Fluid Mechanics*, 239:85–104, 2017. ISSN 0377-0257. doi: 10.1016/j.jnnfm.2016.12.002.

[36] R J Poole. The deborah and weissenberg numbers. *Rheol. Bull*, 53(2):32–39, 2012.

[37] R J Poole, M A Alves, and P J Oliveira. Purely elastic flow asymmetries. *Physical Review Letters*, 99: 164503, 10 2007. doi: 10.1103/PhysRevLett.99.164503.

[38] J Ramsay, M J H Simmons, A Ingram, and E H Stitt. Mixing performance of viscoelastic fluids in a kenics km in-line static mixer. *Chemical Engineering Research and Design*, 115:310–324, 2016. ISSN 0263-8762. doi: https://doi.org/10.1016/j.cherd.2016.07.020.

[39] G N Rocha, R J Poole, M A Alves, and P J Oliveira. On extensibility effects in the cross-slot flow bifurcation. *Journal of Non-Newtonian Fluid Mechanics*, 156:58–69, 2009. ISSN 0377-0257. doi: https://doi.org/10.1016/j.jnnfm.2008.06.008.

[40] J Soulages, M S N Oliveira, P C Sousa, M A Alves, and G H McKinley. Investigating the stability of viscoelastic stagnation flows in t-shaped microchannels. *Journal of Non-Newtonian Fluid Mechanics*, 163:9–24, 2009. ISSN 0377-0257. doi: https://doi.org/10.1016/j.jnnfm.2009.06.002.

[41] E S Szalai, M M Alvarez, and F J Muzzio. Laminar mixing: A dynamical systems approach, 11 2003. Wiley Online Books.

[42] H A Castillo Sánchez, M R Jovanović, S Kumar, A Morozov, V Shankar, G Subramanian, and H J Wilson. Understanding viscoelastic flow instabilities: Oldroyd-b and beyond. *Journal of Non-Newtonian Fluid Mechanics*, 302:104742, 2022. ISSN 0377-0257. doi: https://doi.org/10.1016/j.jnnfm.2022.104742.

[43] S Varchanis, C C Hopkins, A Q Shen, J Tsamopoulos, and S J Haward. Asymmetric flows of complex fluids past confined cylinders: A comprehensive numerical study with experimental validation. *Physics of Fluids*, 32:053103, 5 2020. ISSN 1070-6631. doi: 10.1063/5.0008783. doi: 10.1063/5.0008783.

[44] S Varchanis, J Tsamopoulos, A Q. Shen, and S J. Haward. Reduced and increased flow resistance in shear-dominated flows of oldroyd-b fluids. *Journal of Non-Newtonian Fluid Mechanics*, 300:104698, 2022. ISSN 0377-0257. doi: 10.1016/j.jnnfm.2021.104698.